*Acta Oceanol. Sin.*, 2021, Vol. 40, No. 7, P. 142–158
https://doi.org/10.1007/s13131-021-1813-3
http://www.aosocean.com
E-mail: ocean2@hyxb.org.cn

# Possible triggering relationship of six $M_w > 6$ earthquakes in 2018–2019 at Philippine archipelago

Qiu Zhong[1, 2, 3*], Yangfan Deng[3, 4], Zhigang Peng[3], Lingyuan Meng[5]

[1] Key Laboratory of Ocean and Marginal Sea Geology, South China Sea Institute of Oceanology, Innovation Academy of South China Sea Ecology and Environmental Engineering, Chinese Academy of Sciences, Guangzhou 510301, China

[2] Southern Marine Science and Engineering Guangdong Laboratory (Guangzhou), Guangzhou 511458, China

[3] School of Earth and Atmospheric Sciences, Georgia Institute of Technology, Atlanta, GA 30332, USA

[4] State Key Laboratory of Isotope Geochemistry, Guangzhou Institute of Geochemistry, Chinese Academy of Sciences, Guangzhou 510640, China

[5] China Earthquake Networks Center (CENC), Beijing 100045, China

Received 1 December 2020; accepted 31 December 2020



**Abstract**

Philippine archipelago (PA) has strong background seismicity, but there is no systematic study of earthquake triggering in this region. There are six earthquakes ($M_w > 6$) occurred between 2018/12/29 and 2019/09/29 in PA, which provides an excellent opportunity to investigate the triggering relationship among these events. We calculate the static Coulomb stress changes of the first five events, and find that the local seismicity after the 2018/12/29 $M_w$ 7.0 earthquake is mostly associated with positive Coulomb stress changes, including the 2019/05/31 $M_w$ 6.1 event, suggesting a possible triggering relationship. However, we cannot rule out the dynamic triggering mechanism, due to increased microseismicity in both positive and negative stress change regions, and an incomplete local catalog, especially right after the first $M_w$ 7.0 mainshock. The dynamic stresses from these $M_w >$ 6 events are large enough (from 5 kPa to 3 532 kPa) to trigger subsequent events, but a lack of seismicity and waveform evidence does not support delayed dynamic triggering among these events, even the shortest time interval is less than 24 hours. In the past 45 years, the released seismic energy shows certain peaks every 5–10 years. However, earthquakes with $M_w > 6.0$ were relatively infrequent between 2004 and 2018 at PA. Hence, it is possible that several regions are relatively late in their earthquake cycles, which would enhance their susceptibility of being triggered by earthquakes at nearby and regional distances.

**Key words:** static triggering, dynamic triggering, seismicity, ETAS model, Philippine archipelago

**Citation:** Zhong Qiu, Deng Yangfan, Peng Zhigang, Meng Lingyuan. 2021. Possible triggering relationship of six $M_w > 6$ earthquakes in 2018–2019 at Philippine archipelago. Acta Oceanologica Sinica, 40(7): 142–158, doi: 10.1007/s13131-021-1813-3

## 1 Introduction

Although the physical mechanism of earthquake triggering is still in debate (Freed, 2005), there are increasing reports on earthquakes triggered by occurrence of another earthquake at nearby (i.e., aftershocks; King and Deves, 2015) or long-range distances (i.e., remotely triggered seismicity; Hill and Prejean, 2015; Pankow and Kilb, 2020). The latter occurs at distances greater than a few fault lengths, and appears to be a common feature after very large earthquakes. For example, the periodical seismicity at Mount Wrangell, Alaska was triggered by surface waves of the 2004 $M_w$ 9.1 Sumatra earthquake (West et al., 2005). Other regions such as Tibet, Southwest China, and the Parkfield-Cholame section of the San Andreas Fault (SAF) in California also showed triggered seismicity (either shallow earthquakes or deep tectonic tremor) after this earthquake (Ghosh et al., 2009; Peng et al., 2009; Lei et al., 2011; Yao et al., 2015; Li et al., 2019). The seismicity at Fangshan Pluton near Beijing was remotely triggered by the 2004 Sumatra mainshock, the 2012 $M_w$ 8.6 Indian Ocean earthquake and other recent large earthquakes in Asia (Wu et al., 2012; Wang et al., 2015). In addition to large distant earthquakes, moderate-size earthquakes are also capable of dynamically triggering earthquakes or tremor at near-field or intermediate distant ranges (e.g., within several hundred kilometers) (Brodsky and Prejean, 2005; Guilhem et al., 2010; Meng and Peng, 2014; Wallace et al., 2017; Peng et al., 2015, 2018; Enescu et al., 2016; Ross et al., 2019).

While most remotely triggered seismicity has small magnitudes, sometimes moderate-size events can be triggered at regional and teleseismic distances (e.g., Pollitz et al., 2012; Johnson and Burgmann, 2016; Wallace et al., 2017). These remotely

Foundation item: The National Natural Science Foundation of China under contract Nos 41704049, 41890813, 91628301 and 41974068; the Chinese Academy of Sciences under contract Nos QYZDY-SSW-DQC005 and 133244KYSB20180029; the foundation of Southern Marine Science and Engineering Guangdong Laboratory (Guangzhou) under contract No. GML2019ZD0205; the foundation of Youth Innovation Promotion Association, Chinese Academy of Sciences under contract No. YIPA2018385; the United States National Science Foundation under contract No. EAR-1736197; the Foundation of Science Foundation for the Earthquake Resilience of China Earthquake Administration under contract No. XH20072.
*Corresponding author, E-mail: qiuzhong@scsio.ac.cn

triggered events normally occurred a few hours to days later (i.e., delayed dynamic triggering), rather than during and/or immediately after the passage of the surface wave of distant mainshock (Parsons and Velasco, 2011). Temporal changes of microseismicity between the first distant mainshock and the subsequent moderate-size event can be used to evaluate whether delayed dynamic triggering could occur (Anderson et al., 1994; Papadopoulos, 2002; Yao et al., 2015; Walter et al., 2015; Johnson and Bürgmann, 2016; Castro et al., 2019).

On the other hand, static triggering (i.e., triggering of seismicity by stress changes due to static stress or permanent fault displacement) has been identified for several decades (King and Deves, 2015). Generally, a positive correlation is found between static stress changes of recent large earthquakes and the spatial distributions of aftershocks, especially those occurred at neighboring faults (e.g., King et al., 1994; Lin and Stein, 2004; Meng and Peng, 2014). For example, King et al. (1994) found a clear increase of aftershock activity at regions with clear Coulomb stress increase after the 1992 $M_w$ 7.3 Landers earthquake, including the $M_w$ 6.3 Big Bear earthquake occurred ~3 h later away from the Landers rupture zone. Based on a matched filter technique, Meng et al. (2013) found a statistically significant decrease in shallow seismicity along the creeping section of the SAF following the 2003 $M_w$ 6.5 San Simeon mainshock, which correlates well with the negative static stress changes (i.e., stress shadow). A similar reduction of low-frequency earthquakes in the lower crust was also found following the same mainshock (Shelly and Johnson, 2011).

Most recent studies on earthquake triggering are conducted at plate-boundary regions or plate interiors with dense seismic instrumentations (e.g., Peng and Gomberg, 2010; Hill and Prejean, 2015; King and Deves, 2015). Only a few studies focused on seismically active region in Southeast Asia. For example, Bansal et al. (2016) found a few isolated regions of triggered activities in Southeast Asia and around the Indian Ocean following the 2012/04/11 $M_w$ 8.6 Indian Ocean earthquake. But it is still not clear how widespread triggered earthquakes can be observed in this region.

In this study, we conduct a systematic search for triggered seismicity around Philippine archipelago (PA). This region is seismically active, and the focal depth of earthquakes distributes from the upper crust to the mantle transition zone (Fig. 1). We focus on six earthquakes with magnitude $M_w > 6$ occurred at PA during 2018/12/29 to 2019/09/29 (GCMT catalog: 2018/12/29, $M_w$ = 7.0; 2019/03/08, $M_w$ = 6.1; 2019/04/22, $M_w$ = 6.1; 2019/04/23, $M_w$ = 6.4; 2019/05/31, $M_w$ = 6.1; 2019/09/29, $M_w$ = 6.2; see details in Table 1). In particular, there are two earthquakes striking in less than 24 h on 2019/04/22 and 2019/04/23

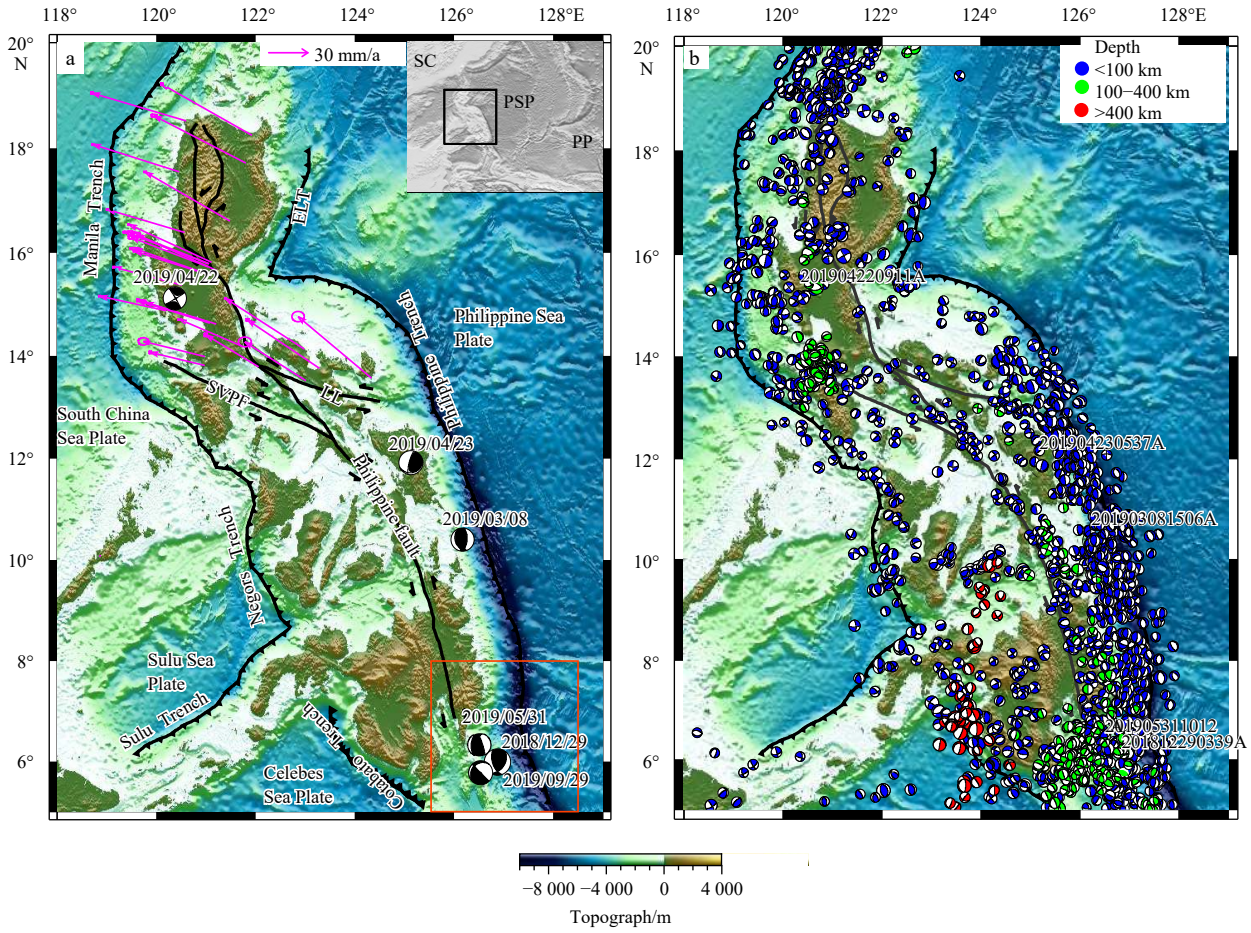


**Fig. 1.** The tectonic background (a) and focal mechanisms of earthquakes (b) at Philippines archipelago (PA). The purple lines and circles indicate the GPS velocity and errors, with respect to the Eurasian Plate. The velocity ranges from 4.9 cm/a to 8.5 cm/a (Yu et al., 2013). The main tectonic features are modified from Aurelio et al. (2017), and Wu et al. (2017). The focal mechanism of the six earthquakes and others (1976–2019) are obtained from the GCMT catalog. The red box in a marks the zoom-in region plotted in Fig. 2. LL: Legaspi Lineament; SVPF: Verde Passage Fault-Sibuyan Sea Fault; SC: South China; PSP: Philippine Sea Plate; PP: Pacific Plate.

**Table 1.** The detailed information of these six earthquakes based on GCMT catalog

| No. | Date | Latitude[1)] | Longitude[1)] | Depth[1)]/km | $M_w$ | Str1/dip1/rake1/(°)[2)] | Str2/dip2/rake2/(°) |
|---|---|---|---|---|---|---|---|
| 1 | 2018/12/29 | 5.48°N | 127.05°E | 60 | 7.0 | 34/46/134 | 160/59/55 |
| 2 | 2019/03/08 | 10.37°N | 126.13°E | 17 | 6.1 | 160/36/69 | 5/57/104 |
| 3 | 2019/04/22 | 15.02°N | 120.34°E | 10 | 6.1 | 329/86/–3 | 59/87/–176 |
| 4 | 2019/04/23 | 11.79°N | 125.37°E | 61 | 6.4 | 70/21/144 | 194/78/73 |
| 5 | 2019/05/31 | 6.15°N | 126.70°E | 78 | 6.1 | 197/30/125 | 338/66/72 |
| 6 | 2019/09/29 | 5.52°N | 126.66°E | 63 | 6.2 | 226/21/–179 | 135/90/–69 |

Notes: [1)] Earthquake location refers to the local catalog. [2)]Primary fault geometry used in Coulomb stress change calculation.

(Fig. 1). The shortest distance between these six earthquakes is less than 100 km. Such a close space-time distribution provides a great opportunity to study possible interaction/triggering among these events.

## 2 Tectonic setting and background seismicity

The tectonic setting of PA is complex (Ringenbach et al., 1993), and the deformation is dominated by the subduction zones of opposite polarities (Fig. 1). To the east, the Pacific Plate (PP) subducts beneath the Philippine Sea Plate (PSP), while the west part of the PSP subducts below the archipelago along the west-dipping East Luzon Trough and Philippine Trench (PT). To the west, four subduction systems dip east or southeast, namely from north to south: (1) Manila Trench (MT) where the South China Sea (SCS) oceanic lithosphere subducts underneath the archipelago; (2) and (3) the Negros and Sulu Trenches where the Sulu Sea oceanic lithosphere subducts underneath the archipelago; and (4) the Cotabato Trench where the Celebes Sea oceanic lithosphere underplates the archipelago (Chen et al., 2015; Aurelio et al., 2017; Wu et al., 2017).

Within the PA, the strike-slip Philippine Fault (PF) cut through the archipelago with ~1 200 km length and an approximately NNW–SSE direction, accommodating the trench-parallel motion from the oblique convergence (Aurelio, 2000). This left-lateral strike-slip fault has a long-term slip rate of 2.4–4.0 cm/a but is mostly locked (Yu et al., 2013), except in the central portion where surface creep has been observed (Yang et al., 2018). There are two large fault branches of the PF, the Legaspi Lineament (LL) and the Sibuyan Verde Passage Fault (SVPF). The later fault spreads from the PF and extends westward near the MT, whereas the former connects the PFZ and the PT. These two faults connect the PF and oppositely-verging subduction systems (Fig. 1).

The GPS data shows the horizontal velocities of PA gradually decrease from north to south along the MT at rates of 8.5–4.9 cm/a in the west-northwest direction, with respect to the Eurasian Plate (Yu et al., 2013). Based on the Global Centroid Moment Tensor (GCMT) catalog, shallow earthquakes (depth < 100 km) are widely distributed through the entire archipelago, while intermediate earthquake (depth 100–400 km) are mostly located at the south part of MT and south part of PT. Deep-focus earthquakes (depth > 400 km) along the subducted PSP slab are featured as a linear distribution at the southernmost part of PA (Fig. 1).

## 3 Static Coulomb stress changes from the 2018–2019 $M_w > 6$ sequences

Here we calculate static Coulomb stress changes generated by five $M_w > 6$ events from 2018 to 2019 in the study region using the Coulomb 3.3 software (Lin and Stein, 2004; Toda et al., 2005, 2011). Coulomb stress changes are computed based on the following equation:

$$\Delta\sigma_c = \Delta\tau_s + \mu'\Delta\sigma_n, \quad (1)$$

where $\mu'$ is the effective friction coefficient, $\Delta\tau_s$ and $\Delta\sigma_n$ are shear and normal stress changes, respectively, depending on the assumed parameters of the receiver fault. Here we use $\mu' = 0.4$ (King et al., 1994),

In this study, we use the USGS finite slip distribution model of the 2018/12/29 $M_w$ 7.0 event as the source fault of the first event (2018/12/29, $M_w$ 7.0). We choose the nodal plane from the GCMT solution (Ekström et al., 2012) according to the subduction zone geometry of the rest events (Table 1) as the source and receiver faults (Table 1, strike1/dip1/rake1). Because static stress changes drop rapidly with distances (i.e., inversely proportional to the cube of distance), here we only compute static Coulomb stress change of the first event (2018/12/29, $M_w$ 7.0) on the receiver faults of the last two events (2019/05/31, $M_w$ 6.1 and 2019/09/29, $M_w$ 6.2), which occurred within 100 km of the first event.

Figure 2 shows the map view of Coulomb stress changes on the preferred receiver faults at their hypocentral depths (78 km and 63 km, respectively). The preferred receiver fault was set be the primary nodal planes (Table 1, strike1/dip1/rake1) of the fifth (2019/05/31, $M_w$ 6.1) and sixth (2019/09/29, $M_w$ 6.2) events. The 2019/05/31 $M_w$ 6.1 event occurred at the region where the Coulomb stress increase is ~19 kPa (Table 2), suggesting a possible triggering relationship. The 2019/09/29 $M_w$ 6.2 event occurred at the region with < 5 kPa (1 kPa) Coulomb stress increase (Table 2). The detailed static Coulomb change induced by every event to the subsequent events are shown in Table 2.

In order to examine the influence of different value of the friction coefficient on the final stress change, we vary its value from 0 to 1, resulting in a very minor change (16–23 kPa) in the peak Coulomb stress change at the hypocentral region of the fifth event (2019/05/31, $M_w$ 6.1). Similarly, the corresponding Coulomb stress changes at the hypocentral region of the sixth event (2019/09/29, $M_w$ 6.2) are 2–7 kPa. We do not calculate Coulomb stress changes for other event pairs, because the corresponding Coulomb stress changes are all very small (< 1 kPa). Considering the uncertainties of the hypocentral depths, we also vary the depths of receiver faults (50 km, 70 km and 90 km) and recompute the Coulomb stress changes. As shown in Fig. A1 , although the stress patterns are different, the peak values at different depths are somewhat similar.

To further investigate the triggering relationship, we examined local microseismicity in this region around the first event (2018/12/29, $M_w$ 7.0). We assumed the microseismicity has the same focal mechanism as the fifth (2019/05/31, $M_w$ 6.1) and sixth (2019/09/29, $M_w$ 6.2) events. As shown in Fig. 3, the seismicity after the event 2018/12/29 mostly occurred in the region with positive Coulomb stress changes, if the receiver fault was set to be the same strike/dip/rake as the 2019/05/31 event. In particular, during 2018/12/29 to 2019/05/31, 74% of events are associated with positive Coulomb stress changes for all events with magnitude $M_w \geqslant 3.5$, while 69% of events with $M_w \geqslant 2.5$ are located in the area of positive Coulomb stress changes (Figs 3c and

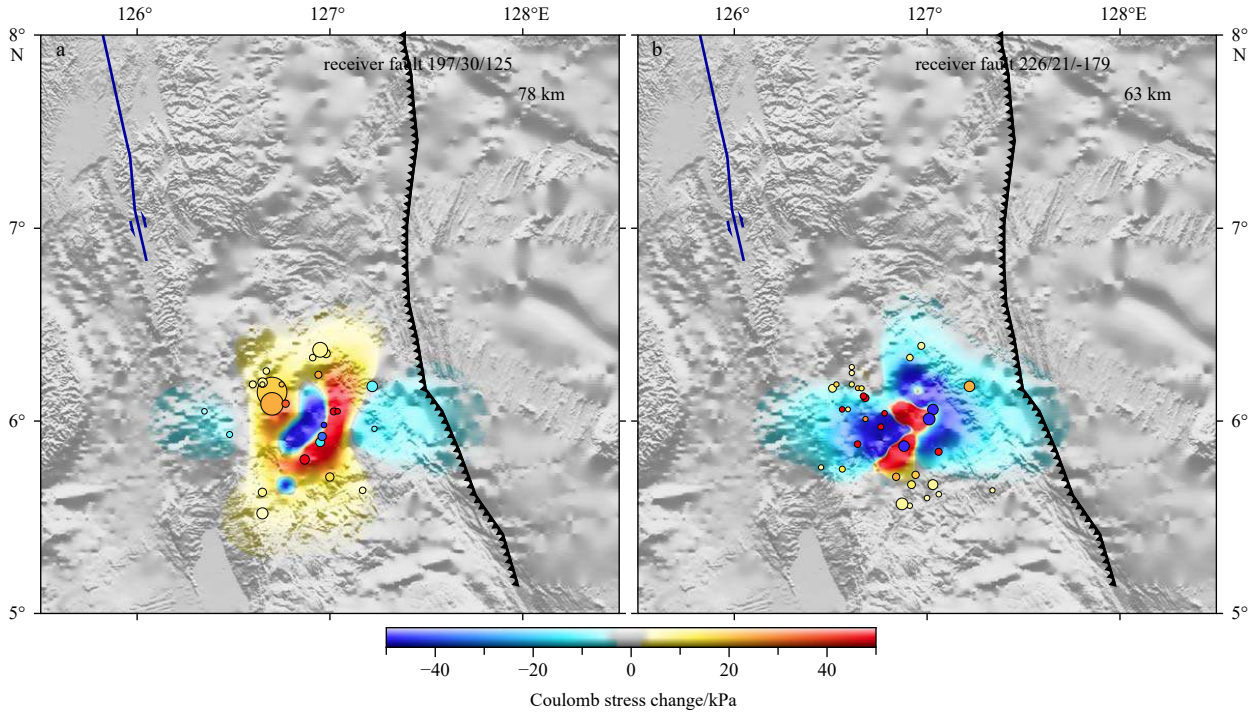


**Fig. 2.** Coulomb stress changes generated by the first event (2018/12/29, $M_w$ 7.0). The source fault model is based on the finite slip model from USGS website (https://earthquake.usgs.gov/earthquakes/eventpage/us2000iyta/finite-fault). The Coulomb stress changes are computed at depth of 78 km and 63 km, receiver fault mechanism was set to be the fifth event (a, c, and e: 2019/05/31, $M_w$ 6.1) and the sixth event (b, d, and f: 2019/09/29, $M_w$ 6.2). Solid circles show the local events ($M_w \geqslant 3.5$) with Coulomb stress change $\Delta\sigma_c \geqslant 5$ kPa, within different depth range ±10 km.

**Table 2.** Static Coulomb stress change of each event to the subsequent events

| Source fault | | Static Coulomb stress change on each receiver fault/kPa | | | | |
|---|---|---|---|---|---|---|
| No. | Date | 2019/03/08 | 2019/04/22 | 2019/04/23 | 2019/05/31 | 2019/09/29 |
| 1 | 2018/12/29 | < 0.1 | < 0.1 | < 0.1 | **19** | **1** |
| 2 | 2019/03/08 | / | < 0.1 | < 0.1 | < 0.1 | < 0.1 |
| 3 | 2019/04/22 | / | / | < 0.1 | < 0.1 | < 0.1 |
| 4 | 2019/04/23 | / | / | / | < 0.1 | < 0.1 |
| 5 | 2019/05/31 | / | / | / | / | 0.4 |
| 6 | 2019/09/29 | / | / | / | / | / |

Note: Bold numbers indicate the static Coulomb stress change ⩾ 1 kPa.

d). It should be noted that the magnitude completeness $M_c$ of local earthquake catalog is $M_c$ = 2.7 (Fig. A2) based on the best-combined method in ZMAP (Wiemer and Wyss, 2000; Woessner and Wiemer, 2005). In addition, we exclude those events located in Coulomb stress changes with absolute value less than 5 kPa, because most previous studies found that Coulomb stress changes above such threshold are capable of triggering microseismicity (e.g., Orlecka-Sikora, 2010). If we include all events occurred within 180 km (3 times of the fault length, which is believed to be the stress-influencing zone of an earthquake (King et al., 1994)) of the $M_w$ 7.0 mainshock, we find that 74% and 77% of events with magnitude $M_w \geqslant 2.5$ and $M_w \geqslant 3.5$ were associated with positive Coulomb stress changes, respectively.

## 4 Dynamic stress changes

We estimate the dynamic stress of earthquakes using a surface-wave magnitude $M_s$ relationship following Van Der Elst and Brodsky (2010). In the near-field (distance < 800 km), we first estimate the peak ground velocity (PGV, in unit of cm/s) using

$$\log_{10}\mathrm{PGV} = -2.29 + 0.85M_s - 1.29\log_{10}r, \quad (2)$$

where $r$ is the hypocentral distance (in km). For the far-field (distance > 800 km) dynamic strain, we use the surface wave magnitude relation:

$$\log_{10}A_{20} = M_s - 1.66\log_{10}\Delta - 2, \quad (3)$$

where $A_{20}$ is the displacement in micrometer and $\Delta$ is in degree.

In both cases, we use the moment magnitude from the GCMT catalog, and assume that the surface magnitude $M_s$ is equal to the moment magnitude $M_w$ for the six $M_w$ > 6.0 events (Shearer, 1999). After computing the PGV and $A_{20}$, we use the following equations to estimate the dynamic stress in kPa (Aki and Richards, 2002):

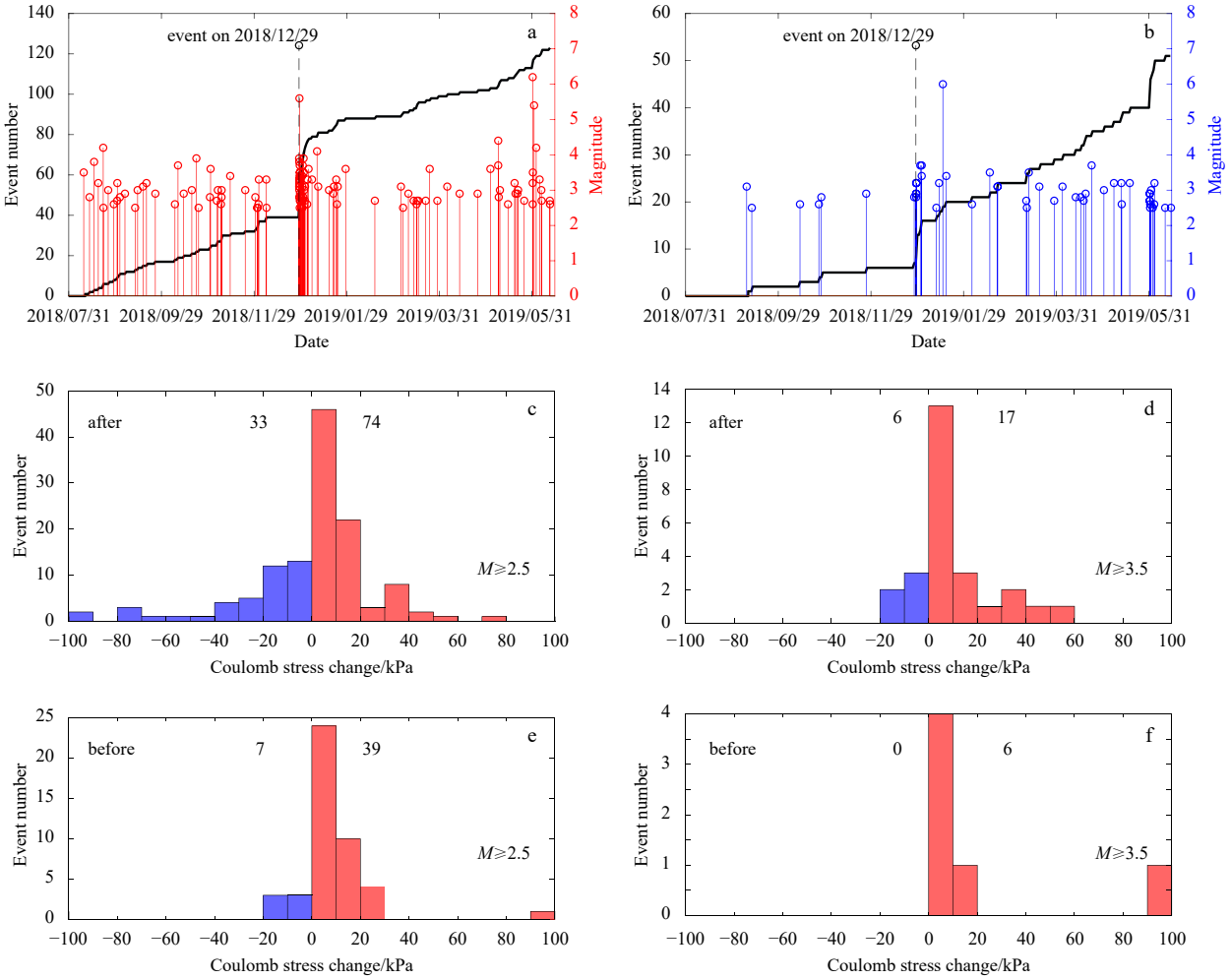


**Fig. 3.** The event distributions and their relationship with Coulomb stress changes of the first event at the regions plotted in Fig. 2. Receiver fault of these local events are set the same as the fifth event (2019/05/31, $M_w$ 6.1). a, b. Accumulated event number (left *y*-axis) and magnitude distributions (right *y*-axis) during 2018/07/31 to 2019/06/15, associated with positive Coulomb stress changes (a) and negative Coulomb stress changes (b); c, d. blue and red bars show the histogram of negative and positive Coulomb stress changes respectively; c. histogram of the $M_w \geqslant 2.5$ earthquakes during 2018/12/29 to 2019/05/31; d. Histogram of the $M_w \geqslant 3.5$ earthquakes during 2018/12/29 to 2019/05/31; e. histogram of $M_w \geqslant 2.5$ events during 2018/07/31 to 2018/12/29; and f. histogram of $M_w \geqslant 3.5$ events during 2018/07/31 to 2018/12/29. The numbers indicate the total count during these periods, and only events with stress change $\geqslant$ 5 kPa are counted. For example, number 6 in f indicates six events during 2018/12/29 to 2019/05/31 at the region with stress change $\geqslant$ 5 kPa. Some events may be missing in the histograms due to the scale of the *x*-axis.

$$\mathrm{PGV} \approx 2\pi A_{20}/T, \tag{4}$$

$$\sigma_d = G \cdot \mathrm{PGV}/V_s, \tag{5}$$

where $\sigma_d$ is dynamic stress, $G$ and $V_s$ are the shear modulus and shear velocity, respectively. Here we assume $V_s$ is 3.5 km/s for 20-s surface wave, and the shear modulus $G$ is 35 GPa (Van Der Elst and Brodsky 2010).

Figure 4 shows the dynamic stress generated by the first event (2018/12/29, $M_w$ 7.0) and the third event (2019/04/22, $M_w$ 6.1). The first earthquake (2018/12/29; $M_w$ 7.0) produced 1 517 kPa peak dynamic stress change to the region where fifth event (2019/05/31, $M_w$ 6.1) occurred. In comparison, the static stress change is ~19 kPa. The corresponding distance between these two events is ~60 km, and the time interval is 154 d. Similarly, the first earthquake generated 3 532 kPa peak dynamic stress change to the region where the six event (2019/09/29, $M_w$ 6.2) occurred. In comparison, the third earthquake (2019/04/22, $M_w$ 6.1) produced ~18 kPa stress change in the region where the next large event—the fourth event (2019/04/23, $M_w$ 6.4) occurred within 24 h. The detailed dynamic stresses induced by each event are listed in Table 3.

Next we examine the local seismicity and waveform data in between these six events to further evaluate their possible triggering relationship. Figure 5 shows the seismicity variation during the six events. Specifically, after the first event (2018/12/29, $M_w$ 7.0), we do not observe any obvious seismicity increase at Regions A, B, and C, which are 1°×1° squares centered around the rest mainshocks (Fig. 4). Similarly, there is no seismicity increase after the second event (2019/03/08, $M_w$ 6.1) at Regions B, C, and D. In addition, there is no earthquake at the time period between the third event (2019/04/22, $M_w$ 6.1) to the fourth event (2019/04/23, $M_w$ 6.4) at Region C.

To supplement with the catalog analysis, we examine waveforms of two broadband stations (Stations IU.DAV and RM.SZP)

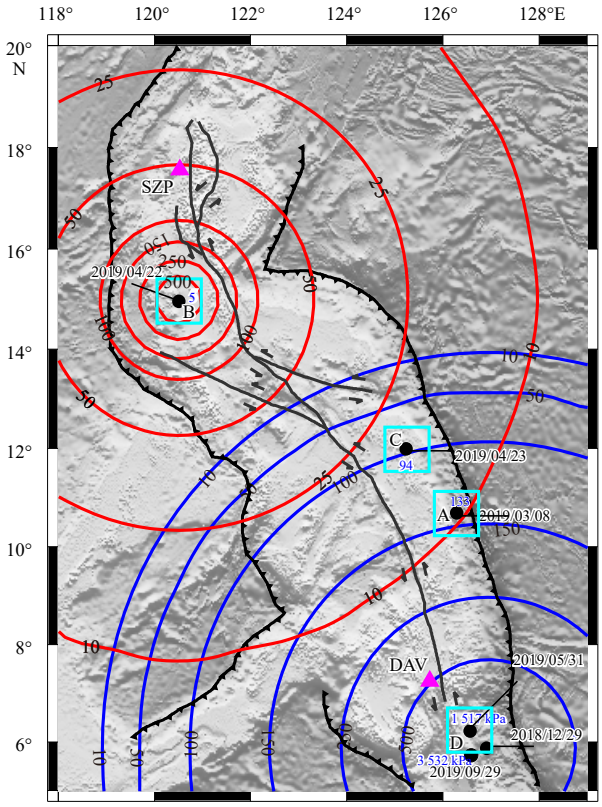


**Fig. 4.** The dynamic stress (in unit of kPa) generated by the event on 2018/12/29 (blue line) and 2019/04/22 (red line). The stress values are marked on the contours. Regions A, B, C, and D are squares with 1°×1° size, and temporal distribution of seismicity within these regions are further plotted in Fig. 5. The locations of two seismic stations (RM.SZP and IU.DAV) are marked, and the corresponding waveforms are plotted in Fig. 6.

with continuous data downloaded from IRIS DMC. Stations IU.DAV and RM.SZP are ~500 km and ~800 km to the epicenter of the fourth event (2019/04/23, $M_w$ 6.4), respectively. We check the raw seismogram, band-pass-filtered envelopes (0.5–2.0 Hz, 4–16 Hz) and spectrogram at these stations during the time period between the third and the fourth events (Fig. 6). We do not include signals in 2–4 Hz due to pronounced background noise in this frequency range, especially at Station IU.DAV. After the third event (2019/04/22, $M_w$ 6.1), there is no obvious earthquake-like signal in the low-frequency (<2 Hz) and high-frequency (4–16 Hz) ranges (except the fourth event), which is consistent with the lack of microearthquakes during this time period as listed in the local catalog. In addition, no earthquake-like signal is observed at Station RM.SZP before or after the fourth event (2019/04/23, $M_w$ 6.4).

## 5 Slip rate inferred from GPS and seismic cycle from seismically released energy

The triggering process could advance or delay the occurrence of an earthquake, depending not only on the triggering stress, but also the frictional state during the earthquake cycle (e.g., Gomberg et al., 1998). Hence, it is important to examine earthquake recurrence time in a particular region to better understand its triggering behavior. However, such estimation is model-dependent and is subjected to observational bias, especially when the recurrence time is longer than the typical instrumentation recording. In this section, we attempt to estimate the slip rate based primarily on GPS observations, in order to better understand the triggering behavior and potential seismic hazard in this region.

Based on the detailed slab geometry of the Manila and Philippine slabs presented in Slab2.0 (Hayes et al., 2018), we project the slip rate on these two slabs (Fig. 7a). According to the resulting slip rates, we can divide the Philippine slab into three sections (southern: 5.0°–11.5°N; central: 11.5°–14.5°N; northern: 14.5°–20.0°N). In order to compare possible seismic cycle with observed seismicity, we plot shallow thrust earthquakes with $M_w > 6$ since 1976 (Fig. 7b). From 1982 to 2004, there are four episodes with at least one $M_w \geqslant 6.4$ earthquake in the central section of Philippine slab. However, in the southern section, there is no earthquake with $M_w \geqslant 6.4$ since 2002, other than the most recent large event on 2018/12/29 with $M_w$ 7.1.

Next, we compute the annual released seismic energy (i.e., summation of yearly energy release) in each section, based on the following empirical relationship between seismic energy $E$ and magnitude $M$ for a single earthquake (Richter, 1958):

$$\log_{10}E = 1.5M + 11.8. \quad (6)$$

Because seismic energy is mostly released by large earthquakes, we calculate the energy release along the three sections (Fig. 7) of the Philippine slab based on the GCMT catalog (with moment magnitudes $M_w$), rather than the regional Philippine catalog (with local magnitudes $M_L$). Figure 8 shows the annual and accumulated seismic energy released by earthquakes since 1976. The southern section shows the peak of annual seismic energy has an apparent cycle of 5–10 years (Fig. 8a). Similarly, the seismic energy in the central section shows an apparent cycle of 5–10 years (Fig. 8b). However, there is a strong peak at 1995, corresponding to a swarm with the largest event on 1995/04/21 ($M_w$ 7.2). It becomes quiet since 1997. The released energy shows strong variations in the northern section of the Philippine slab, which peaks in 1977–1978 during another earthquake swarm (the largest magnitude is $M_w$ 7.3). If we examine the overall seismic

**Table 3.** Dynamic stress change of each event to the subsequent events

| Source fault | | Dynamic stress change on each receiver faults/kPa | | | | |
|---|---|---|---|---|---|---|
| No. | Date | 2019/03/08 | 2019/04/22 | 2019/04/23 | 2019/05/31 | 2019/09/29 |
| 1 | 2018/12/29 | 133 | 5 | 94 | **1 517** | **3 532** |
| 2 | 2019/03/08 | / | 1 | 99 | 28 | 24 |
| 3 | 2019/04/22 | / | / | 18 | 1 | 1 |
| 4 | 2019/04/23 | / | / | / | 34 | 30 |
| 5 | 2019/05/31 | / | / | / | / | **329** |
| 6 | 2019/09/29 | / | / | / | / | / |

Note: Bold numbers indicate the dynamic stress change ⩾ 300 kPa

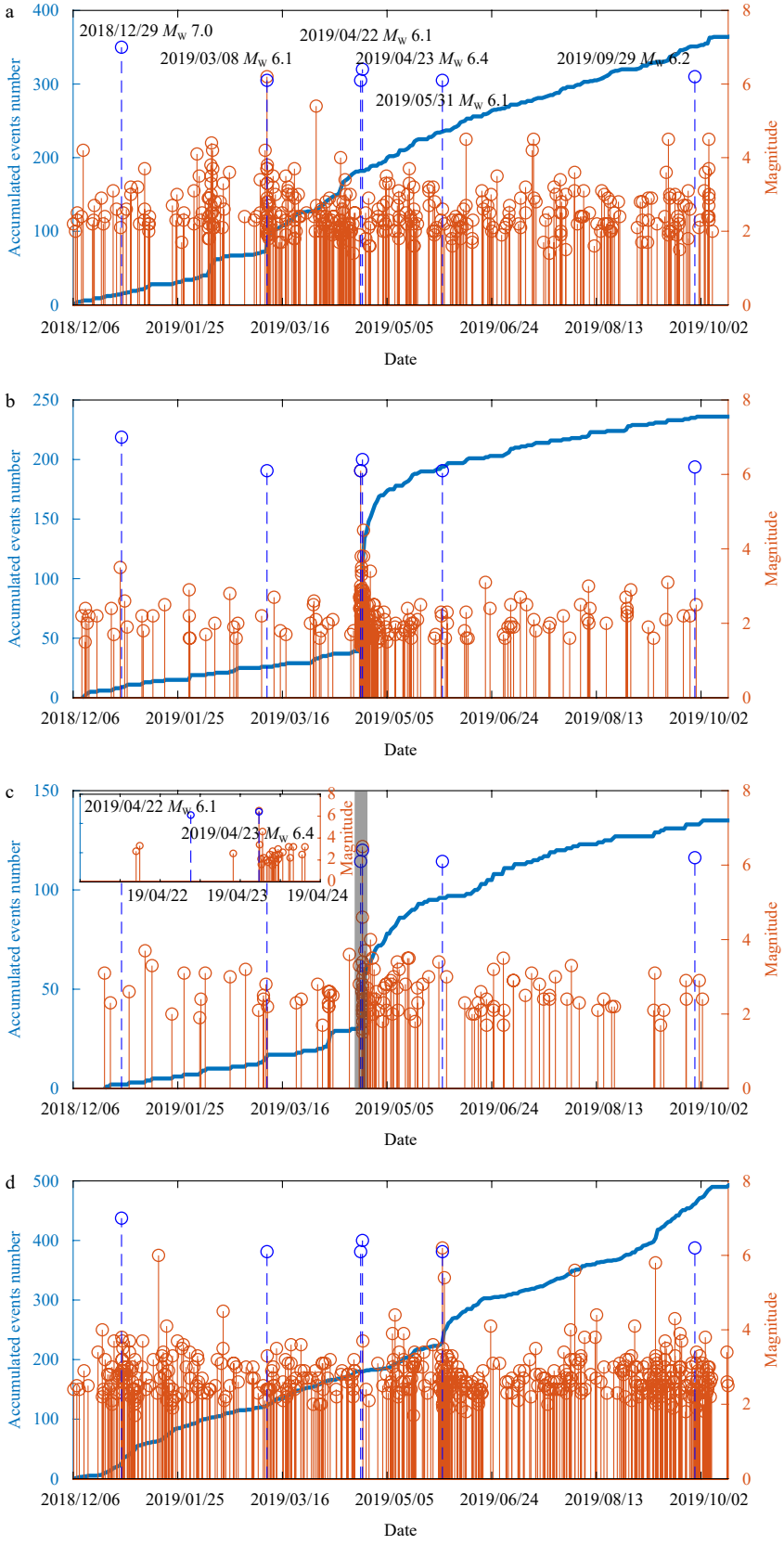


**Fig. 5.** The local seismicity at Regions A, B, C and D as marked in Fig. 4. The left axis is the accumulated events number and the right axis is the magnitude. The occurrence time of the first five earthquakes is marked as dashed blue lines. The insert map of c shows the detailed seismicity between 2019/04/21 to 2019/04/24 (shaded region).

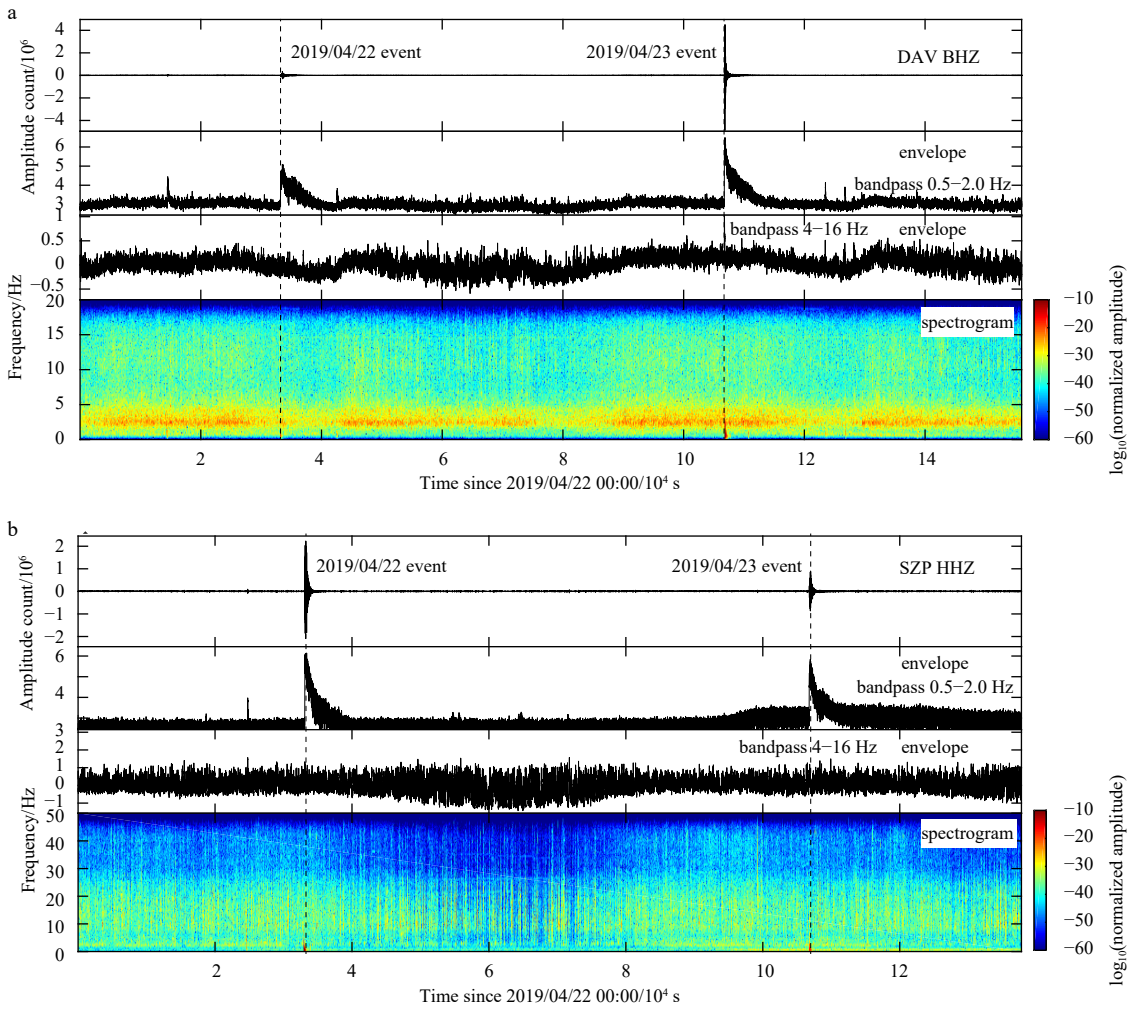


**Fig. 6.** The seismogram, band-passed envelopes (0.5–2.0 Hz, 4–16 Hz) and spectrogram of seismic data recorded at Stations IU.DAV (a) and RM.SZP (b). Their corresponding locations are marked in Fig. 4.

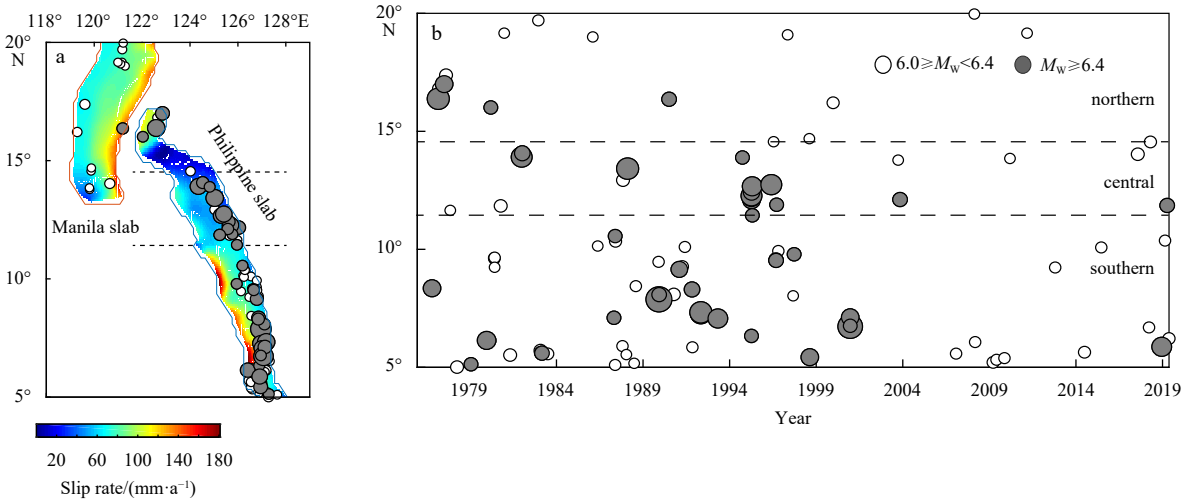


**Fig. 7.** The slip rate estimated from GPS velocity (a) and the distribution of thrust events listed in the GCMT catalog during 1976/01/01 to 2019/12/31 along the Manila and Philippine slabs (b). The Philippine slab can be divided into three sections (southern, central, and northern) according to the slip rate.

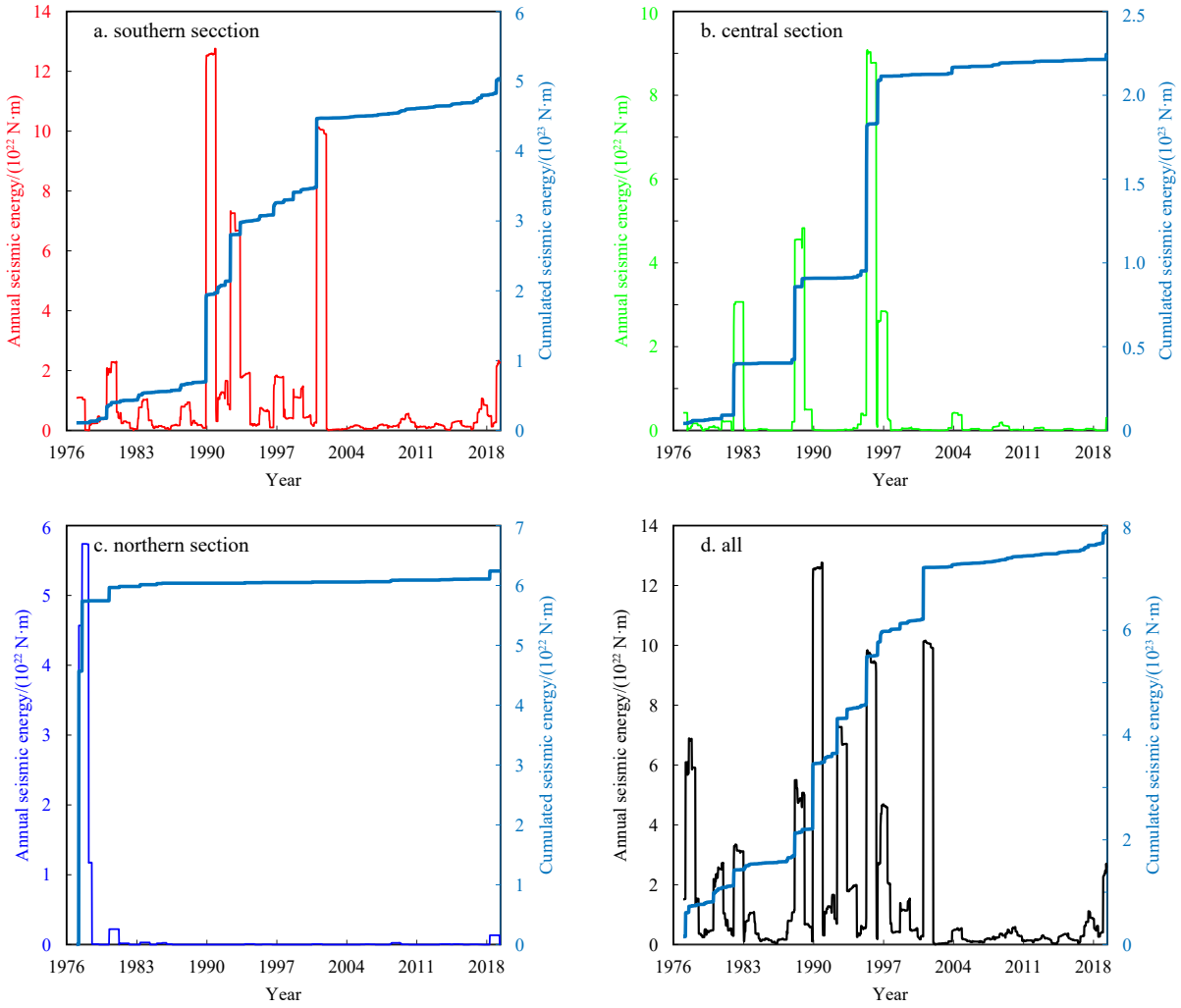


**Fig. 8.** The annual and cumulative seismic energy during 1976/01/01 to 2019/12/31 at the southern section of Philippine slab (5.0°–11.5°N) (a), the central section of Philippine slab (11.5°–14.5°N) (b), the northern section of Philippine slab (14.5°–20.0°N) (c), and all sections (d). The detailed division of Philippine slab is marked in Fig. 7.

energy release (Fig. 8d), it is clear that the entire region is relatively quiet between 2002 and 2018.

## 6 The likelihood of having six $M_w > 6$ events within 274 d

In this section we examine how often it is to observe six $M_w > 6$ events within 274 d, which is the time duration between the first and last $M_w > 6$ events in this region. To do this, we first calculate the background probability of all events with $M_w \geqslant 5$ since 1976/01/01 as listed in the GCMT catalog (Fig. 9) based on the space-time epidemic-type aftershock sequence (ETAS) model (Ogata, 1988; Zhuang et al., 2002, 2004). The corresponding parameters are shown in Table 4. Then, we de-cluster these events according to the probability and space-time clustering. Because the ETAS model only considers those close in space and time as triggered events (i.e., aftershocks), earthquakes that are remotely triggered (i.e., in long-range distances) are considered as independent events (i.e., background events).

Figure 9 shows the background probability of $M_w > 6$ events since 1976, and the events with background probability $P_b \geqslant 0.5$. The swarms are declustered in this step, such as the July 2010 sequence. The recent 6 events all have high probability as background (independent) events with probability $P_b \geqslant 0.9$. Finally, we compute the time spans between adjacent six $M_w > 6$ events with probability $P_b \geqslant 0.5$. As shown in Fig. 9c, only eight groups have their time spans for six adjacent events less than 274 d, including the most recent sequence. For the entire time period, the duration of six adjacent background events show an apparent arc shape, which increases since 1976 and peaks around 2008.

## 7 Discussion

Triggered earthquakes occur as a result of the redistribution of stress (e.g., static, dynamic or quasi-static stress changes) imparted by previous earthquakes (Freed, 2005). In this study, we examined the triggering relationship and possible triggering mechanisms associated with six $M_w > 6$ earthquakes occurred in the PA within ~9 months in 2018–2019. The distances between the first event (2018/12/29, $M_w$ 7.0) to the fifth (2019/05/31, $M_w$ 6.1) and the sixth (2019/09/29, $M_w$ 6.2) event are both less than 100 km. The Coulomb stress changes imparted by the 2018/12/29 $M_w$ 7.0 event are ~19 kPa and < 5 kPa at the locations of the 2019/05/31 $M_w$ 6.1 and 2019/09/29 $M_w$ 6.2 events, respectively. In comparison, the dynamic stress changes are ~1 517 kPa and 3 532 kPa, much larger than static stress changes.

It is worth noting that, when we assumed the receiver fault

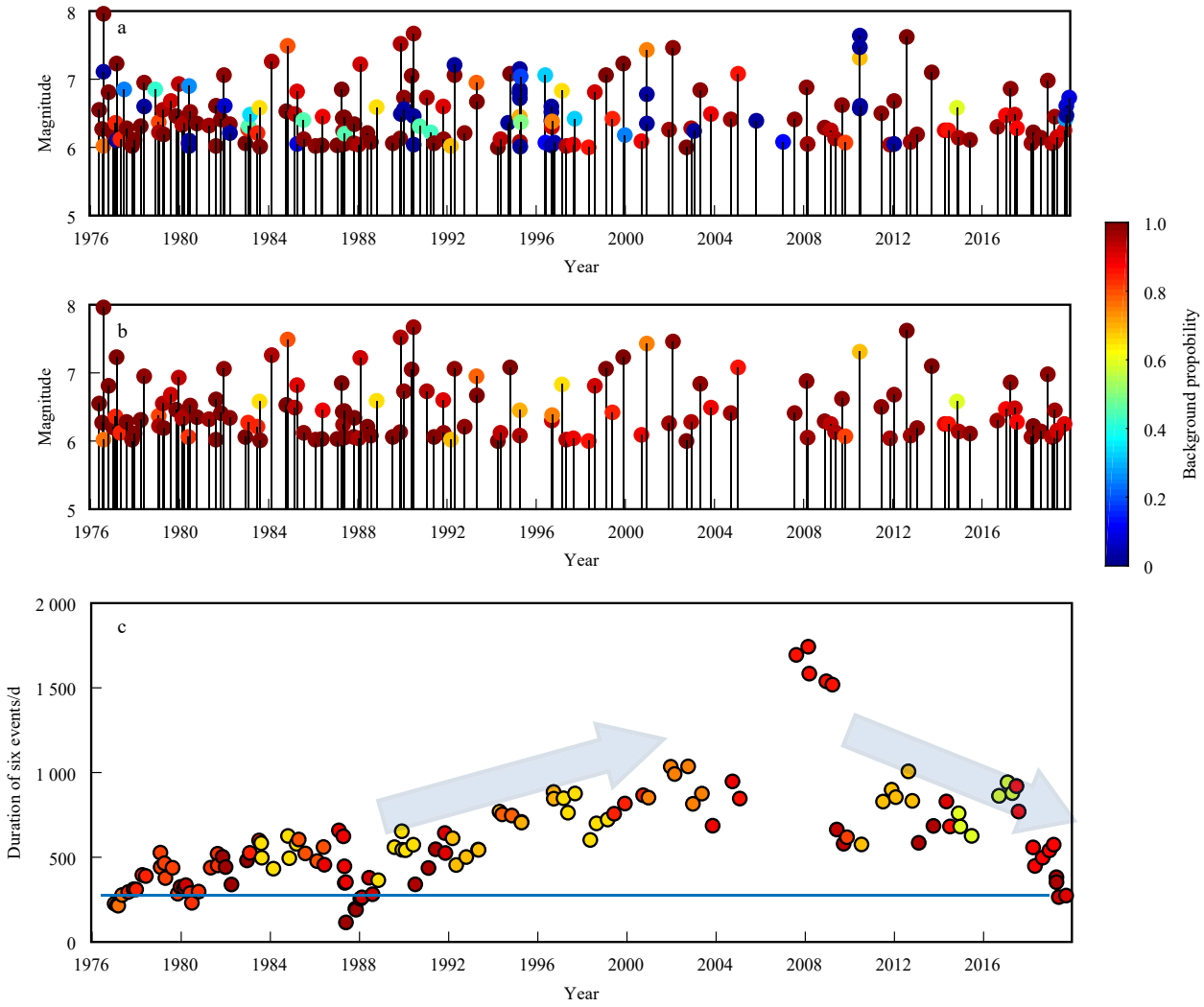


**Fig. 9.** The probability of background seismicity from the space-time ETAS model. a. The background probability of $M_w > 6$ events along the PA from 1976/01/01 to 2019/12/31 based on the GCMT catalog; b. the events with background probability $P_b \geqslant 0.5$; and c. the duration of six adjacent $M_w > 6$ events with background probability $P_b \geqslant 0.5$. The probability value represents the lowest one of the 6 adjacent events. The solid line mark the duration of 274 d for the recent six $M_w > 6$ events. The two arrows indicate the trend of the duration of 6 high probability adjacent events.

**Table 4.** ETAS model parameters

| | Parameter | | | | | | | |
|---|---|---|---|---|---|---|---|---|
| | $\mu$ | $A$ | $c$ | $\alpha$ | $p$ | $d$ | $q$ | $\gamma$ |
| Value | 1.02 | 0.13 | 0.06 | 1.42 | 1.13 | 0.004 | 1.94 | 1.41 |

planes of the microseismicity the same as the sixth event (2019/09/29, $M_w$ 6.1), only 44% events locate in the positive Coulomb stress change region (Fig. A3). We can infer that the triggered microseismicity by the first event (2018/12/29, $M_w$ 7.0) are mostly thrust fault event on the fifth event's fault plane. And events on the strike-slip fault of the sixth event (2019/12/29, $M_w$ 6.1) are unlikely to be triggered by the first event (2018/12/29, $M_w$ 7.0), including the sixth large earthquake (2019/09/29, $M_w$ 6.1). We also calculated Coulomb stress changes on optimal thrust and normal faults (Fig. A4). The local events location also shows a better consistency with the Coulomb stress change when the receiver fault plane is set as the optimal thrust fault within each depth range (Figs A4a and b. 40–60 km; Figs A4c and d. 60–80 km; Figs A4e and f. 80–100 km).

We note that static stress change is able to permanently advance or delay an earthquake nucleation depending on its sign. Hence, it can result in either seismicity rate increase or decrease (Belardinelli et al., 2003; Toda et al., 2012; Meng et al., 2013). On the other hand, dynamic stress change can only result in a transient increase of seismicity rate following the mainshock (Kilb, 2003). After the 2018/12/29 $M_w$ 7.0 event, microseismicity increased in both positive and negative Coulomb stress change regions (Figs 3e–f), which would favor the dynamic stress triggering model. However, we did not observe a clear increase of microseismicity around the epicenter of the fifth event (2019/05/31, $M_w$ 6.1) right after the first event (2018/12/29, $M_w$ 7.0) (Fig. A5). Such a transient increase of microseismicity has been often used as the proxy to link the first mainshock and subsequent triggering event (e.g., Anderson et al., 1994; Walter et al., 2015; Johnson and Bürgmann, 2016; Castro et al., 2019). It is possible that such lack of instantaneously triggered event could be due to missing events right after a mainshock (e.g., Peng et al., 2007; Enescu et al., 2007; Meng and Peng, 2014). Hence, although the fifth event

(2019/05/31, $M_w$ 6.1) occurred in the region with positive static stress change (and therefore can be explained by static stress triggering), we cannot completely rule out the possibility of delayed dynamic triggering.

We note the dynamic stress changes generated by the first event are in the range of 5–3 532 kPa (Table 3). If we assume 5 kPa as the dynamic triggering threshold (Brodsky and Prejean, 2005; Johnson and Bürgmann, 2016; Aiken and Peng, 2014), then one could argue that these $M_w > 6$ events could dynamically trigger each other, with certain time delays. Hence, it is reasonable to argue that the number of nuclear points closer to failure in 2018–2019 are more than at other times, favoring the occurrence of remote dynamic triggering (e.g., Pollitz et al., 2012; Johnson and Bürgmann, 2016). This argument is consistent with the observation that there were no other groups of six $M_w > 6$ events observed within 274 d since the 1980s with high background probability (Fig. 9), and a relative lack of $M_w > 6$ events since 2004 (Fig. 7).

However, we did not find any evidence of change in local seismicity to support the delayed dynamic triggering between these events. Similarly, even though the time interval between the third (2019/04/22, $M_w$ 6.1) and the fourth (2019/04/23, $M_w$ 6.4) event is less than 24 hours, the local seismicity and available waveform data did not provide any additional evidence for dynamic triggering. Again, we note that due to the lack of locally available seismic data, we cannot expand the local catalog with techniques like template matching to detect smaller magnitude events for additional evidence of delayed dynamic triggering (e.g., Johnson and Bürgmann, 2016; Walter et al., 2015; Castro et al., 2019). Building a better local catalog can help to better understand their triggering relationship, but this is beyond the scope of this study.

In the stochastic model of earthquake prediction, the six $M_w > 6$ events are all independent (background rate > 0.9) events, which implies no triggering relationship between each other. This result is inconsistent with the Coulomb stress change model. However, the two models are based on two different theories. Resent research are trying to combine stochastic model (ETAS or STEP) with physical model (Coulomb model) (Bach and Hainzl, 2012; Steacy et al., 2014; Reverso et al., 2018). And result shows that Coulomb stress model performed better on predicting more distant aftershocks (Bach and Hainzl, 2012).

Finally, we note that plate convergence rate is almost the same at Philippine slab and Manila slab (Smoczyk et al., 2013). However, Philippine slab has more $M_w > 6$ thrust events than Manila slab. The difference between the Philippine and Manila slabs are quite small, in terms of the strike, dip, and velocity structures imaged by seismic tomography (Hayes et al., 2018; Fan and Zhao, 2019). However, the age of the Philippine slab is older than that of the Manila slab (Müller et al., 2008). In addition, the expected recurrence time of shallow thrust events ($M_w$ 6.4) event is 5–10 years, resulting in much more expected events than being observed. This suggests that many sections on both slabs either creep aseismically (due to weak coupling between two plates), or remain fully locked so that the accumulated strains will be released in future large events. Recent studies suggest that at least portions of Manila slab have high coupling (Lin et al., 2015), and are capable of producing large megathrust earthquakes with significant tsunamis (Sepúlveda et al., 2019; Qiu et al., 2019). Hence, it is important to continuously monitor both subduction zones with both seismic and geodetic instruments to better understand their seismic behaviors.

## 8 Conclusions

In this study we examined the triggering relationship of six earthquakes with $M_w > 6$ occurred in PA from 2018/12/29 to 2019/09/29. We computed the static Coulomb stress change and dynamic stress changes between these events. In addition, we estimated the slip rate and the released seismic energy along the PT and MT. Based on our analysis, we drew the following conclusions. (1) The fifth event (2019/05/31, $M_w$ 6.0) was likely triggered by static stress changes of the first event (2018/12/29, $M_w$ 7.0). 74% of local events with $M_w \geqslant 3.5$ after the first event is associated with the positive Coulomb stress change, including the fifth $M_w > 6.0$ event. We did not find any evidence for static triggering of the sixth event (2019/09/29, $M_w$ 6.1). However, we cannot rule out the delayed dynamic triggering mechanism, because microseismicity increased in regions with both positive and negative Coulomb stress change, and the local catalog may be incomplete, especially right after the first event (2018/12/29, $M_w$ 7.0). (2) The dynamic stress for each event is strong enough to trigger the subsequent earthquake, especially the stress induced by the first one which is also the largest event. However, we did not find any evidence of dynamic triggering (from both local catalogs and seismic recordings at regional distances) among these earthquakes, including two earthquakes occurring within 24 hours. (3) The released seismic energy shows certain peaks at the Philippine slab after every 5–10 years. However, earthquakes with $M_w > 6.0$ were relatively infrequent between 2004 and 2018. The space-time ETAS model also reveals that it is infrequent to observe six $M_w > 6$ independent (background) events (i.e., not being considered as traditional aftershocks) within 274 d. Hence, with a relatively low background rate in the past ten years, there are more regions closer to failure, making them easier to be triggered at nearby and regional distances.

***Acknowledgements***

The seismic waveform data analyzed in this study are downloaded from the IRIS Data Management Center (http://ds.iris.edu/mda/IU/DAV and http://ds.iris.edu/mda/RM/SZP). The local catalog is downloaded from https://www.phivolcs.dost.gov.ph/index.php/earthquake/earthquake-information3. We appreciate GCMT provides the earthquake catalog. Some figures were prepared using the public domain GMT software (Wessel and Smith, 1998).

## References

Aiken C, Peng Zhigang. 2014. Dynamic triggering of microearthquakes in three geothermal/volcanic regions of California. Journal of Geophysical Research: Solid Earth, 119(9): 6992–7009, doi: 10.1002/2014JB011218

Aki K, Richard P G. 2002. Quantitative Seismology. 2nd ed. Sausalito, CA: University Science Books

Anderson J G, Brune J N, Louie J N, et al. 1994. Seismicity in the western Great Basin apparently triggered by the Landers, California, earthquake, 28 June 1992. Bulletin of the Seismological Society of America, 84(3): 863–891

Aurelio M A. 2000. Shear partitioning in the Philippines: Constraints from Philippine fault and global positioning system data. Island Arc, 9(4): 584–597, doi: 10.1046/j.1440-1738.2000.00304.x

Aurelio M A, Dianala J D B, Taguibao K J L, et al. 2017. Seismotectonics of the 6 February 2012 $M_W$ 6.7 Negros Earthquake, central Philippines. Journal of Asian Earth Sciences, 142: 93–108, doi: 10.1016/j.jseaes.2016.12.018

Bach C, Hainzl S. 2012. Improving empirical aftershock modeling based on additional source information. Journal of Geophysical Research: Solid Earth, 117(B4): B04312, doi: 10.1029/2011JB008901

Bansal A R, Yao Dongdong, Peng Zhigang, et al. 2016. Isolated regions of remote triggering in South/Southeast Asia following

the 2012 $M_W$ 8.6 Indian Ocean earthquake. Geophysical Research Letters, 43(20): 10654–10662, doi: 10.1002/2016GL069955

Belardinelli M E, Bizzarri A, Cocco M. 2003. Earthquake triggering by static and dynamic stress changes. Journal of Geophysical Research: Solid Earth, 108(B3): 2135

Brodsky E E, Prejean S G. 2005. New constraints on mechanisms of remotely triggered seismicity at Long Valley Caldera. Journal of Geophysical Research: Solid Earth, 110(B4): B04302, doi: 10.1029/2004JB003211

Castro A F P, Dougherty S L, Harrington R M, et al. 2019. Delayed dynamic triggering of disposal-induced earthquakes observed by a dense array in Northern Oklahoma. Journal of Geophysical Research: Solid Earth, 124(4): 3766–3781, doi: 10.1029/2018JB017150

Chen Pofei, Olavere E A, Wang Chenwei, et al. 2015. Seismotectonics of Mindoro, Philippines. Tectonophysics, 640–641: 70–79

Ekström G, Nettles M, Dziewoński A M. 2012. The global CMT project 2004–2010: Centroid-moment tensors for 13, 017 earthquakes. Physics of the Earth and Planetary Interiors, 200–201: 1–9, doi: 10.1016/j.pepi.2012.04.002

Enescu B, Mori J, Miyazawa M. 2007. Quantifying early aftershock activity of the 2004 mid-Niigata Prefecture earthquake ($M_W$6.6). Journal of Geophysical Research: Solid Earth, 112(B4): B04310

Enescu B, Shimojo K, Opris A, et al. 2016. Remote triggering of seismicity at Japanese volcanoes following the 2016 *M*7.3 Kumamoto earthquake. Earth, Planets and Space, 68: 165, doi: 10.1186/s40623-016-0539-5

Fan Jianke, Zhao Dapeng. 2019. P-wave anisotropic tomography of the central and southern Philippines. Physics of the Earth and Planetary Interiors, 286: 154–164, doi: 10.1016/j.pepi.2018.12.001

Freed A M. 2005. Earthquake triggering by static, dynamic, and postseismic stress transfer. Annual Review of Earth and Planetary Sciences, 33: 335–367, doi: 10.1146/annurev.earth.33.092203.122505

Ghosh A, Vidale J E, Peng Zhigang, et al. 2009. Complex nonvolcanic tremor near Parkfield, California, triggered by the great 2004 Sumatra earthquake. Journal of Geophysical Research: Solid Earth, 114(12)

Gomberg J, Beeler N M, Blanpied M L, et al. 1998. Earthquake triggering by transient and static deformations. Journal of Geophysical Research: Solid Earth, 103(B10): 24411–24426, doi: 10.1029/98JB01125

Guilhem A, Peng Zhigang, Nadeau R M. 2010. High-frequency identification of non-volcanic tremor triggered by regional earthquakes. Geophysical Research Letters, 37(16): L16309, doi: 10.1029/2010GL044660

Hayes G P, Moore G L, Portner D E, et al. 2018. Slab2, a comprehensive subduction zone geometry model. Science, 362(6410): 58–61, doi: 10.1126/science.aat4723

Johnson C W, Bürgmann R. 2016. Delayed dynamic triggering: Local seismicity leading up to three remote $M \geqslant 6$ aftershocks of the 11 April 2012 *M*8.6 Indian Ocean earthquake. Journal of Geophysical Research: Solid Earth, 121(1): 134–151, doi: 10.1002/2015JB012243

Hill D P, Prejean S G. 2015. 4.11-Dynamic triggering. Treatise on Geophysics, 4: 273–304

Kilb D. 2003. A strong correlation between induced peak dynamic Coulomb stress change from the 1992 *M*7.3 Landers, California, earthquake and the hypocenter of the 1999 *M*7.1 Hector Mine, California, earthquake. Journal of Geophysical Research: Solid Earth, 108(B1): ESE 3-1–ESE 3-7, doi: 10.1029/2001JB000678

King G C P, Deves M H. 2015. Fault interaction, earthquake stress changes, and the evolution of seismicity. Treatise on Geophysics, 4: 225–255

King G C P, Stein R S, Lin Jian. 1994. Static stress changes and the triggering of earthquakes. Bulletin of the Seismological Society of America, 84(3): 935–953

Lei Xinglin, Xie Chaodi, Fu Bihong. 2011. Remotely triggered seismicity in Yunnan, southwestern China, following the 2004 $M_w$ 9.3 Sumatra earthquake. Journal of Geophysical Research: Solid Earth, 116(B8): B08303, doi: 10.1029/2011JB008245

Li Lu, Wang Baoshan, Peng Zhigang, et al. 2019. Dynamic triggering of microseismicity in Southwest China following the 2004 Sumatra and 2012 Indian Ocean Earthquakes. Journal of Asian Earth Sciences, 176: 129–140, doi: 10.1016/j.jseaes.2019.02.010

Lin Jian, Stein R S. 2004. Stress triggering in thrust and subduction earthquakes and stress interaction between the southern San Andreas and nearby thrust and strike-slip faults. Journal of Geophysical Research: Solid Earth, 109(B2): B02303

Lin Jingyi, Wu Wennan, Lo C L. 2015. Megathrust earthquake potential of the Manila subduction system: revealed by the seismic moment tensor element Mrr. Terrestrial, Atmospheric and Oceanic Sciences, 26(6): 619–630, doi: 10.3319/TAO.2013.04.29.01(TC)

Meng Xiaofeng, Peng Zhigang. 2014. Seismicity rate changes in the Salton Sea Geothermal Field and the San Jacinto Fault Zone after the 2010 $M_w$ 7.2 El Mayor-Cucapah earthquake. Geophysical Journal International, 197(3): 1750–1762, doi: 10.1093/gji/ggu085

Meng Xiaofeng, Peng Zhigang, Hardebeck J L. 2013. Seismicity around Parkfield correlates with static shear stress changes following the 2003 $M_W$6.5 San Simeon earthquake. Journal of Geophysical Research: Solid Earth, 118(7): 3576–3591, doi: 10.1002/jgrb.50271

Müller R D, Sdrolias M, Gaina C, et al. 2008. Age, spreading rates, and spreading asymmetry of the world's ocean crust. Geochemistry, Geophysics, Geosystems, 9(4): Q04006

Ogata Y. 1988. Statistical models for earthquake occurrences and residual analysis for point processes. Journal of the American Statistical Association, 83(401): 9–27, doi: 10.1080/01621459.1988.10478560

Orlecka-Sikora B. 2010. The role of static stress transfer in mining induced seismic events occurrence, a case study of the Rudna mine in the Legnica-Glogow Copper District in Poland. Geophysical Journal International, 182(2): 1087–1095, doi: 10.1111/j.1365-246X.2010.04672.x

Pankow K L, Kilb D. 2020. Going beyond rate changes as the sole indicator for dynamic triggering of earthquakes. Scientific Reports, 10: 4120, doi: 10.1038/s41598-020-60988-2

Papadopoulos G A. 2002. The Athens, Greece, earthquake ($M_S$ 5.9) of 7 September 1999: an event triggered by the Izmit, Turkey, 17 August 1999 earthquake?. Bulletin of the Seismological Society of America, 92(1): 312–321, doi: 10.1785/0120000805

Parsons T, Velasco A. 2011. Absence of remotely triggered large earthquakes beyond the mainshock region. Nature Geoscience, 4: 312–316, doi: 10.1038/ngeo1110

Peng Zhigang, Fry B, Chao K, et al. 2018. Remote triggering of microearthquakes and tremor in New Zealand following the 2016 $M_W$ 7.8 Kaikōura earthquake. Bulletin of the Seismological Society of America, 108(3B): 1784–1793, doi: 10.1785/0120170327

Peng Zhigang, Gomberg J. 2010. An integrated perspective of the continuum between earthquakes and slow-slip phenomena. Nature Geoscience, 3: 599–607, doi: 10.1038/ngeo940

Peng Zhigang, Shelly D R, Ellsworth W L. 2015. Delayed dynamic triggering of deep tremor along the Parkfield-Cholame section of the San Andreas Fault following the 2014 M6.0 South Napa earthquake. Geophysical Research Letters, 42(19): 7916–7922, doi: 10.1002/2015GL065277

Peng Zhigang, Vidale J E, Ishii M, et al. 2007. Seismicity rate immediately before and after main shock rupture from high-frequency waveforms in Japan. Journal of Geophysical Research: Solid Earth, 112: B03306, doi: 10.1029/2006JB004386

Peng Zhigang, Zhao Peng. 2009. Migration of early aftershocks following the 2004 Parkfield earthquake. Nature Geoscience, 2: 877–881, doi: 10.1038/ngeo697

Pollitz F, Stein R, Sevilgen V, et al. 2012. The 11 April 2012 east Indian Ocean earthquake triggered large aftershocks worldwide. Nature, 490: 250–253, doi: 10.1038/nature11ence504

Qiu Qiang, Li Linlin, Hsu Y J, et al. 2019. Revised earthquake sources along Manila trench for tsunami hazard assessment in the

South China Sea. Natural Hazards and Earth System Sciences, 19(7): 1565–1583, doi: 10.5194/nhess-19-1565-2019

Reverso T, Steacy S, Marsan D. 2018. A hybrid ETAS-Coulomb approach to forecast spatiotemporal aftershock rates. Journal of Geophysical Research: Solid Earth, 123(11): 9750–9763, doi: 10.1029/2017JB015108

Richter C F. 1958. Elementary Seismology. San Francisco: W H Freeman and Co Bailey Bros & Swinfen Ltd

Ringenbach J C, Pinet N, Stéphan J F, et al. 1993. Structural variety and tectonic evolution of strike-slip basins related to the Philippine Fault System, northern Luzon, Philippines. Tectonics, 12(1): 187–203, doi: 10.1029/92TC01968

Ross Z E, Trugman D T, Hauksson E, et al. 2019. Searching for hidden earthquakes in Southern California. Science, 364(6442): 767–771, doi: 10.1126/science.aaw6888

Sepúlveda I, Liu P L F, Grigoriu M. 2019. Probabilistic tsunami hazard assessment in South China Sea with consideration of uncertain earthquake characteristics. Journal of Geophysical Research: Solid Earth, 124(1): 658–688, doi: 10.1029/2018JB016620

Shearer P M. 1999. Introduction to Seismology. Cambridge: Cambridge University Press

Shelly D R, Johnson K M. 2011. Tremor reveals stress shadowing, deep postseismic creep, and depth-dependent slip recurrence on the lower-crustal San Andreas fault near Parkfield. Geophysical Research Letters, 38(13)

Smoczyk G M, Hayes G P, Hamburger M W, et al. 2013. Seismicity of the earth 1900–2012 Philippine Sea plate and vicinity. USGS Open-File Report: 2010-1083-M. Reston, VA, USA: U.S. Geological Survey

Steacy S, Gerstenberger M, Williams C, et al. 2014. A new hybrid Coulomb/statistical model for forecasting aftershock rates. Geophysical Journal International, 196(2): 918–923, doi: 10.1093/gji/ggt404

Toda S, Stein R S, Beroza G C, et al. 2012. Aftershocks halted by static stress shadows. Nature Geoscience, 5(6): 410–413, doi: 10.1038/ngeo1465

Toda S, Stein R S, Richards-Dinger K, et al. 2005. Forecasting the evolution of seismicity in southern California: Animations built on earthquake stress transfer. Journal of Geophysical Research: Solid Earth, 110(B5): B05S16, doi: 10.1029/2004JB003415

Toda S, Stein R S, Sevilgen V, et al. 2011. Coulomb 3.3 Graphic-rich deformation and stress-change software for earthquake, tectonic, and volcano research and teaching-user guide. Open-File Report 2011-1060. Reston, VA, USA: U S Geological Survey, doi: 10.3133/ofr20111060

Van Der Elst N J, Brodsky E E. 2010. Connecting near-field and far-field earthquake triggering to dynamic strain. Journal of Geophysical Research: Solid Earth, 115(B7): B07311, doi: 10.1029/2009JB006681

Wallace L M, Kaneko Y, Hreinsdóttir S, et al. 2017. Large-scale dynamic triggering of shallow slow slip enhanced by overlying sedimentary wedge. Nature Geoscience, 10(10): 765–770, doi: 10.1038/ngeo3021

Walter J I, Meng Xiaofeng, Peng Zhigang, et al. 2015. Far-field triggering of foreshocks near the nucleation zone of the 5 September 2012 ($M_W$ 7.6) Nicoya Peninsula, Costa Rica earthquake. Earth and Planetary Science Letters, 431: 75–86, doi: 10.1016/j.epsl.2015.09.017

Wang Wejun, Meng Xiaofeng, Peng Zhigang, et al. 2015. Increasing background seismicity and dynamic triggering behaviors with nearby mining activities around Fangshan Pluton in Beijing, China. Journal of Geophysical Research: Solid Earth, 120(8): 5624–5638, doi: 10.1002/2015JB012235

Wessel P, Smith W H F. 1998. New, improved version of generic mapping tools released. Eos, Transactions American Geophysical Union, 79(47): 579, doi: 10.1029/98EO00426

West M, Sánchez J J, McNutt S R. 2005. Periodically triggered seismicity at mount Wrangell, Alaska, after the Sumatra earthquake. Science, 308(5725): 1144–1146, doi: 10.1126/science.1112462

Wiemer S, Wyss M. 2000. Minimum magnitude of completeness in earthquake catalogs: examples from Alaska, the Western United States, and Japan. Bulletin of the Seismological Society of America, 90(4): 859–869, doi: 10.1785/0119990114

Woessner J, Wiemer S. 2005. Assessing the quality of earthquake catalogues: estimating the magnitude of completeness and its uncertainty. Bulletin of the Seismological Society of America, 95(2): 684–698, doi: 10.1785/0120040007

Wu Wennan, Lo C L, Lin Jingyi. 2017. Spatial variations of the crustal stress field in the Philippine region from inversion of earthquake focal mechanisms and their tectonic implications. Journal of Asian Earth Sciences, 142: 109–118, doi: 10.1016/j.jseaes.2017.01.036

Wu Jing, Peng Zhigang, Wang Weijun, et al. 2012. Comparisons of dynamic triggering near Beijing, China following recent large earthquakes in Sumatra. Geophysical Research Letters, 39(21): L21310

Yang Yinghui, Tsai M C, Hu J C, et al. 2018. Coseismic slip deficit of the 2017 $M_W$ 6.5 Ormoc earthquake that occurred along a creeping segment and geothermal field of the Philippine Fault. Geophysical Research Letters, 45(6): 2659–2668, doi: 10.1002/2017GL076417

Yao Dongdong, Peng Zhigang, Meng Xiaofeng. 2015. Systematical search for remotely triggered earthquakes in Tibetan Plateau following the 2004 $M$ 9.0 Sumatra and 2005 $M$ 8.6 Nias earthquakes. Geophysical Journal International, 201(2): 543–551, doi: 10.1093/gji/ggv037

Yu S B, Hsu Y J, Bacolcol T, et al. 2013. Present-day crustal deformation along the Philippine Fault in Luzon, Philippines. Journal of Asian Earth Sciences, 65: 64–74, doi: 10.1016/j.jseaes.2010.12.007

Zhuang Jiacang, Ogata Y, Vere-Jones D. 2002. Stochastic declustering of space-time earthquake occurrences. Journal of the American Statistical Association, 97(458): 369–380, doi: 10.1198/016214502760046925

Zhuang Jiacang, Ogata Y, Vere-Jones D. 2004. Analyzing earthquake clustering features by using stochastic reconstruction. Journal of Geophysical Research: Solid Earth, 109(B5): B05301

# Appendix

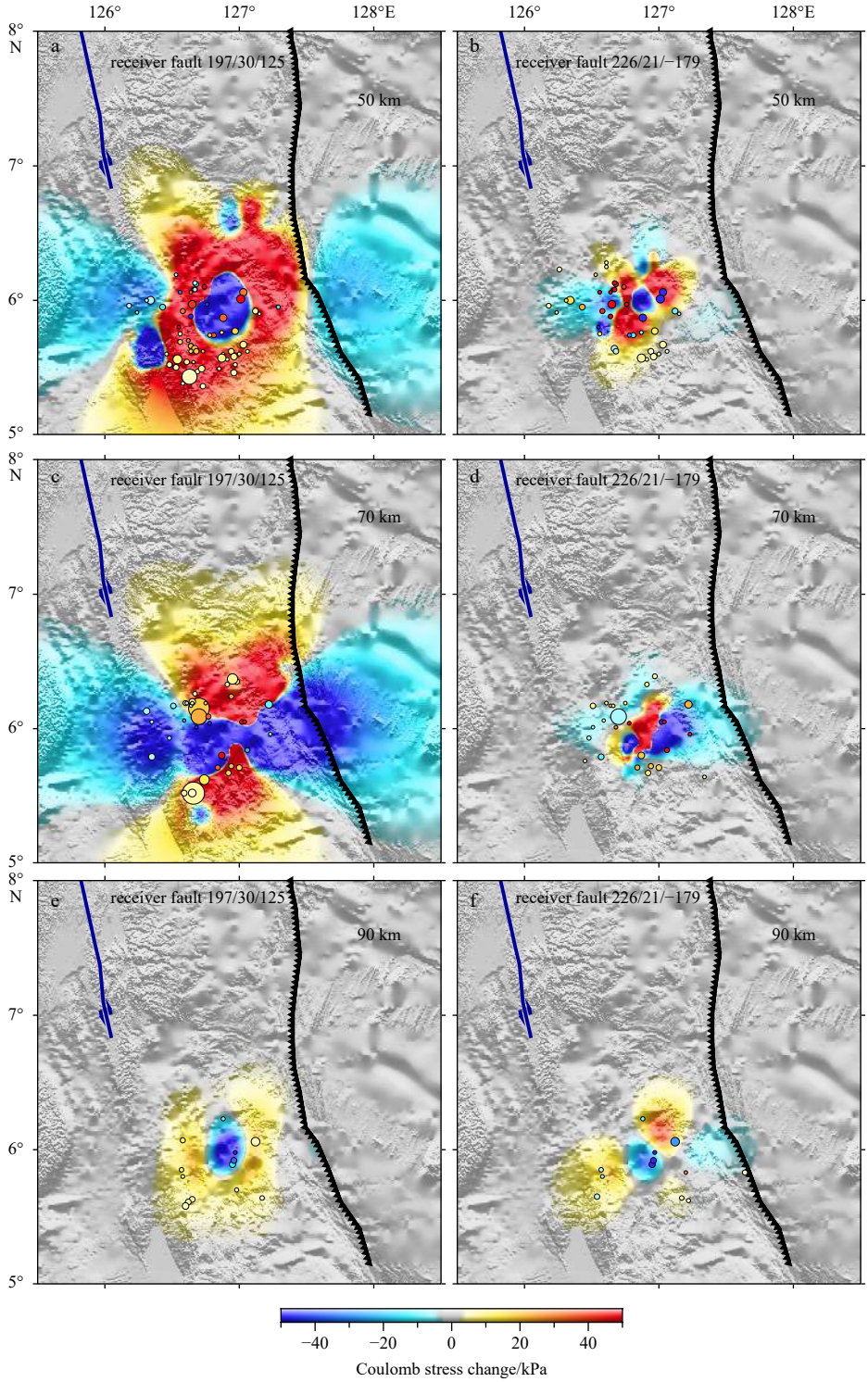


**Fig. A1.** Coulomb stress changes generated by the first event (2018/12/29, $M_w$ 7.0). The source fault model is based on the finite slip model from USGS website (https://earthquake.usgs.gov/earthquakes/eventpage/us2000iyta/finite-fault). The Coulomb stress changes are computed at depth of 50 km, 70 km and 90 km, receiver fault mechanism was set to be the fifth event (a, c, and e: 2019/05/31, $M_w$ 6.1) and the sixth event (b, d, and f: 2019/09/29, $M_w$ 6.2). Solid circles show the local events ($M_w \geqslant 3.5$) with Coulomb stress change $\Delta\sigma_c \geqslant 5$ kPa, within different depth range (a and b: 40–60 km; c and d: 60–80 km; e and f: 80–100 km). Mechanism of the local events was assumed to be the same as the fifth event (a, c, and e: 2019/05/31, $M_w$ 6.1) and the sixth event (b, d, and f: 2019/09/29, $M_w$ 6.2).

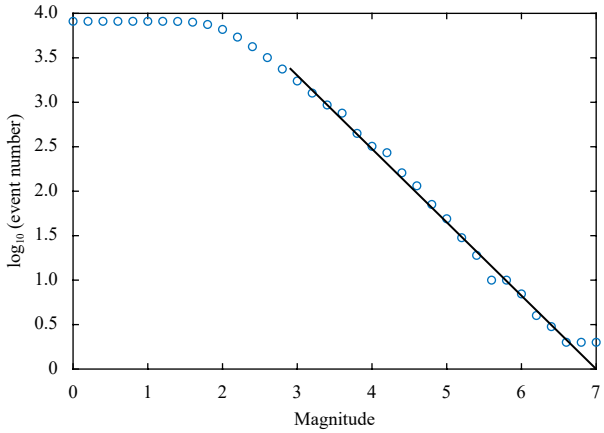


**Fig. A2.** Number of earthquakes versus magnitude of events in the local catalog during 2018/08/01 to 2019/06/15. Blue circles are the raw data, and black line is fitted flowing the Gutenberg-Richter law.

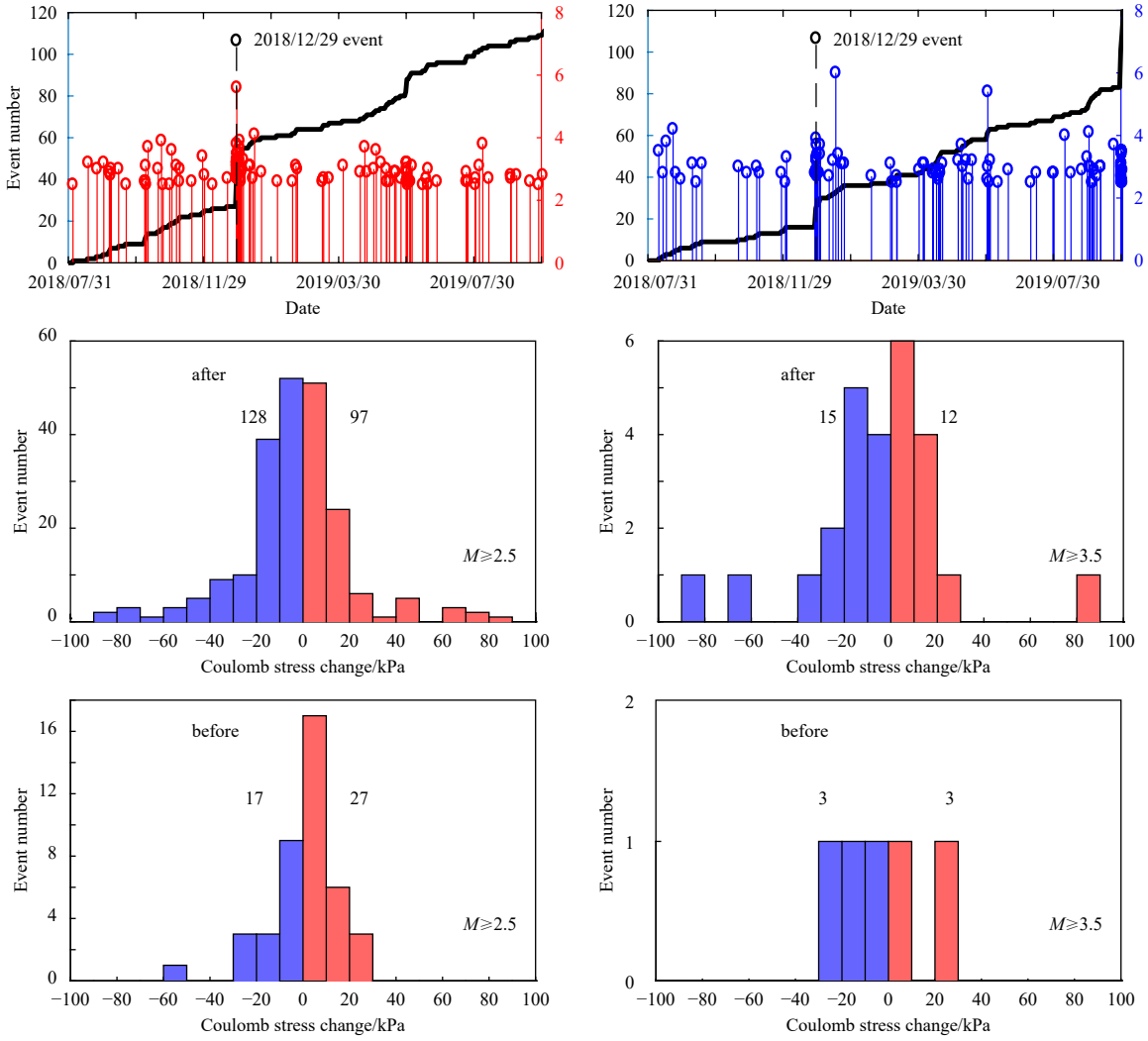


**Fig. A3.** The event distributions and their relationship with Coulomb stress changes of the first event at the regions plotted in Fig. 2. Receiver fault of these local events are set the same as the sixth event (2019/09/29, $M_w$ 6.2). a, b. Accumulated event number (left *y*-axis) and magnitude distributions (right *y*-axis) during 2018/07/31 to 2019/09/29, associated with positive Coulomb stress changes (a) and negative Coulomb stress changes (b); c, d. Blue and red bars show the histogram of negative and positive Coulomb stress changes respectively; c. Histogram of the $M_w \geqslant 2.5$ earthquakes during 2018/12/29 to 2019/09/29; d. Histogram of the $M_w \geqslant 3.5$ earthquakes during 2018/12/29 to 2019/09/29; e. Histogram of $M_w \geqslant 2.5$ events during 2018/07/31 to 2018/12/29; and f. Histogram of $M_w \geqslant 3.5$ events during 2018/07/31 to 2018/12/29. The numbers indicate the total count during these periods, and only events with stress change $\geqslant$ 5 kPa are counted.

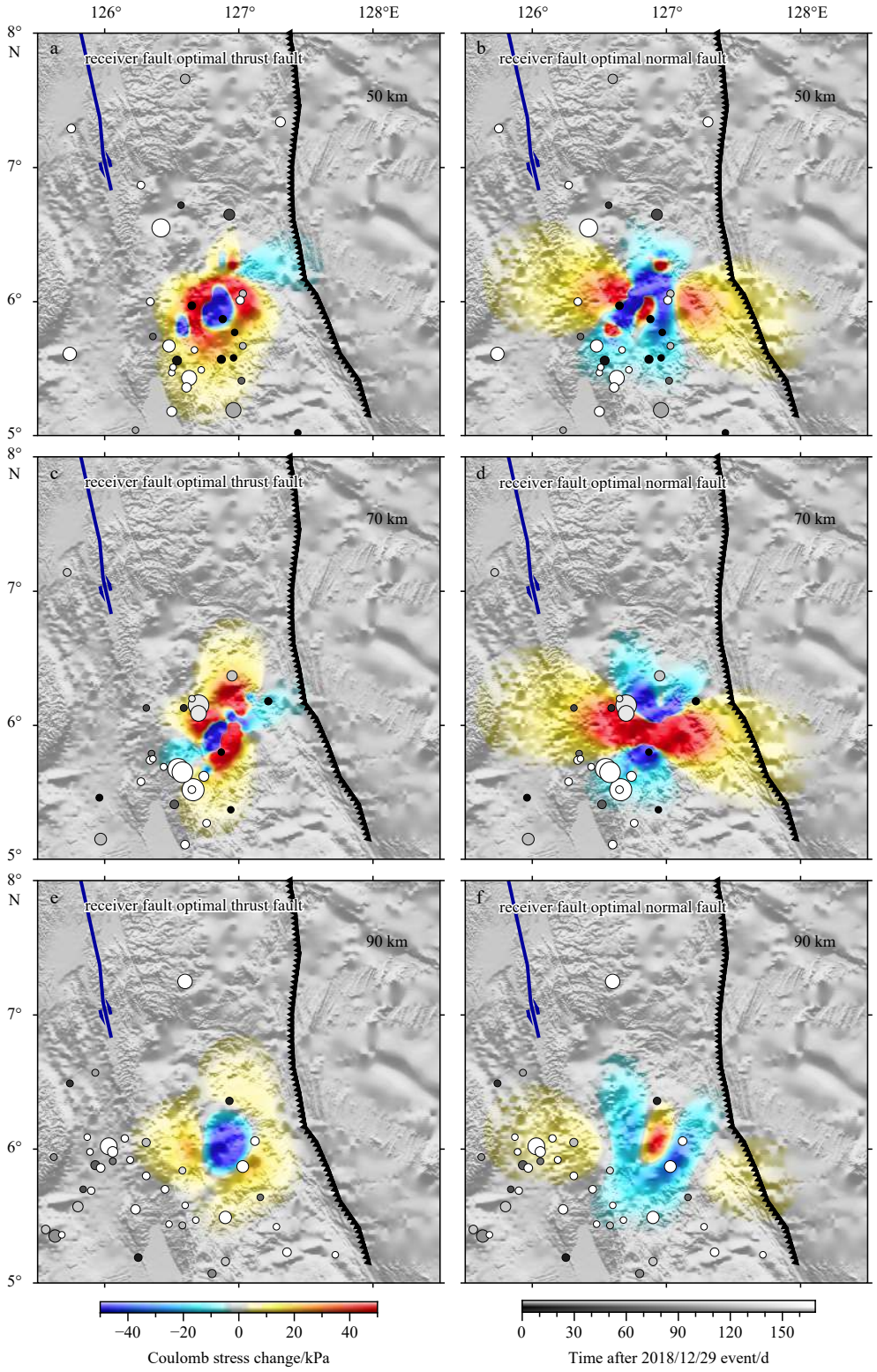


**Fig. A4.** Coulomb stress changes generated by the first event (2018/12/29, $M_w$ 7.0). The source fault model is based on the finite slip model from USGS website (https://earthquake.usgs.gov/earthquakes/eventpage/us2000iyta/finite-fault). The Coulomb stress changes are computed at depth of 50 km, 70 km and 90 km, receiver fault mechanism was set to be the optimal thrust fault (a, c, and e) and optimal normal fault (b, d, and f). Solid circles show the local events within different depth range ±10 km.

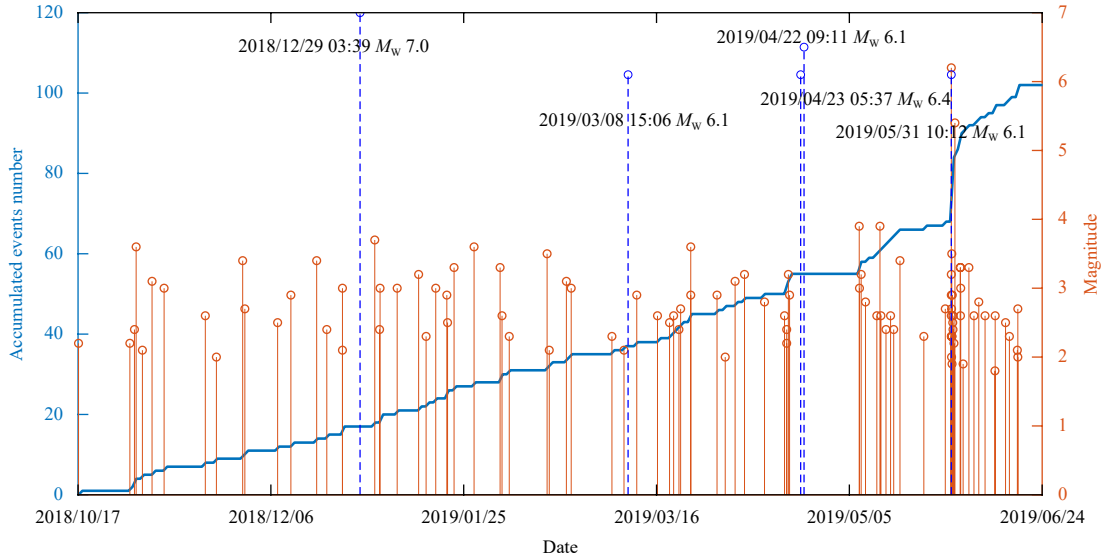


**Fig. A5.** The local seismicity at the 0.5°×0.5° square with the center of the 2019/05/31 event. No instant seismicity increase is observed after 2018/12/29 at this region. The occurrence time of the five earthquakes is marked with dashed blue lines.